Coupling the dynamics of boundary layers and evolutionary dunes

Pablo Ortiz*
University of Granada, Ed. Politecnico, Campus Fuentenueva, 18071 Granada, Spain

Piotr K. Smolarkiewicz†
National Center for Atmospheric Research, Boulder, Colorado 80307, USA

(Received 21 September 2008; revised manuscript received 10 January 2009; published 20 April 2009)

A theoretical formulation and corresponding numerical solutions are presented for fluid flow and sediment transport past evolutionary sand dunes. Time-dependent curvilinear coordinates are employed to fully couple flow aloft with the developing landform. The differential conservation law that defines shape of the lower boundary depends on details of local surface stress, thereby favoring the large eddy simulation of the boundary layer. To shrink the gap between the time scales characteristic of planetary boundary layer flows $O(10^3)$ s and sand dune evolution $O(10^6)$ s, a hypothetical "severe-wind scenario" is adopted with the saltation flux amplified up to 3 orders of magnitude. While the results are largely insensitive to the rescaling, the efficacy of computations is greatly improved. The flux-form partial differential equation for the interface profile—via saltation and sand avalanches—is formulated as an advection-diffusion equation, to facilitate discrete integrations. Numerical experiments verify the adopted theoretical framework by reproducing scaling results reported in the literature. The versatility of the approach is illustrated with evolution of a sandhole—an example of application likely never addressed in the literature, yet realizable in nature.

DOI: 10.1103/PhysRevE.79.041307 PACS number(s): 45.70.−n, 07.05.Tp, 47.57.Gc, 47.55.−t

I. INTRODUCTION

The prediction of fluid flows and cohesionless sediment transport past evolutionary landforms has been a challenge for decades. Among the variety of active landforms, evolutionary dunes are an archetype of fluid/terrain interaction. From the theoretical view point, dunes development and accompanying sand transport is a fundamental dynamical mechanism with challenging detail. In particular, it concerns flows with intricate geometric time-dependent boundary forcings. In practice, however, the two-phase interaction is typically neglected or simplified adopting a quasisteady approximation (QSA). For instance, in [1] the authors report the laboratory investigation of turbulent flows past fixed dunes in 2D, while idealized-model numerical studies of dunes evolution, e.g., [2,3], prescribe the airflow phenomenology. The QSA approach assumes the time scale of flow variability much shorter than that for the dune evolution, so the dune evolution depends parametrically on the boundary layer flow. For example, numerical simulations of barchan and transverse dunes [4,5] employ surface shear stresses provided by a semianalytic solution of a steady-state boundary layer model for three-dimensional (3D) flows past fixed hills. Whereas, calculations of [6] integrate the flow equations past a frozen landform to a steady state, and update the boundary profile subsequently in the frozen flow.

Obviously, in extreme winds the scale-separation assumption is invalid. Furthermore, scale analysis is only discriminating when it identifies terms that cannot be neglected. Since dune/fluid dynamics is governed by complex nonlinear partial differential equations (PDEs), even small-magnitude terms can have a profound impact on the solution. Although the solutions generated with steady and QSA models shed light on the dune dynamic, the complete understanding eludes the efforts. Outstanding examples include the attainability of the equilibrium shape of an isolated barchan dune [4,6] or calving barchan dunes [2]. The details of the genesis and development of barchan dunes [6] or estimating the rates of erosion [4] also call for improving.

In [7], we proposed a "severe-wind scenario" that relaxes the limitations of the quasisteady approximation while fully coupling the two phases of the dune/fluid system. The underlying motivation is the affordability of computational models, resulting from shrinking the gap between the time scales characteristic of planetary boundary layer flows $O(10^3)$ s and sand dune evolution $O(10^6)$ s. In [7] it was realized by amplifying the saltation flux by 3 orders of magnitude. This has a similar effect to increasing the fluid density from air to water, as considered in some laboratory studies, e.g. [8,9]. Although such an arbitrary amplification of the saltation flux precludes a complete physical similarity, an approximate dynamic similarity (substantiated by the results in Secs. III B and III C) can be of practical importance; cf. Sec. 10 in [10].

Predicting sediment transport and bed evolution in severe wind conditions depends on accurate prediction of a flow past complex boundary evolving with the flow itself. We employ a variant of the multiscale computational fluid model EULAG—widely documented in the literature; see [11] for a recent review and a comprehensive list of references—that couples the internal flow with a lower boundary evolving in response to the sand saltation. The key prerequisite facilitating this development is the use of time-dependent curvilinear coordinates [12–14] that accommodate rapid changes in the boundary shape. In consequence of the adopted severe-wind scenario, the geometric difficulty of the two-phase coupling is enhanced by the ubiquity of the turbulence and separating surface planetary boundary layers. Since realistic response of

*portiz@ugr.es
†Corresponding author; smolar@ucar.edu

the sediment-transport model depends crucially on the boundary stress, we employ a large-eddy-simulation (LES) approach with the Smagorinsky-type subgrid-scale turbulence model [15].

The locus of the solid/fluid interface is standardly described by an Eulerian conservation law relating the height of the interface to the divergence of sediment fluxes [4,6,16]. Following developments in [7], we cast the standard equation in an advection-diffusion PDE form, to improve the solution accuracy while simplifying computational procedures. In particular, the saltation fluxes—assumed dominant for dune development—are written as convective fluxes with the effective velocity representing transport rate averaged over the local thickness of the sediment stratum. Sand avalanches—acting as natural slope limiter—are represented as diffusive fluxes, with anisotropic, inhomogeneous diffusion coefficient depending critically on the local slope, cf. [17]. In general, the sediment transport requires a threshold shear velocity for the onset. We employ a modified formula that takes into account the local slope of the interface as well as the direction of the tangential flow. With the rearranged sediment conservation law, the nonoscillatory numerics of EULAG improve the accuracy, stability, and robustness of earlier approximations. We verify the theoretical developments by canonical experiments addressing the scaling laws of a single barchan dune.

The formulation of the coupled fluid and sediment transport model is summarized next. Results of the canonical experiments are discussed in Sec. III. Section IV demonstrates the versatility of the approach and concludes the paper.

II. COUPLED MODEL OF AIR/DUNE INTERACTION

A. Fluid model

A unique feature of EULAG that facilitates the present study is its formulation in generalized time-dependent coordinates

$$(\bar{t},\bar{\mathbf{x}}) \equiv (t,\mathcal{F}(t,\mathbf{x})), \tag{1}$$

where the coordinates $(t,\mathbf{x})$ of the physical domain are assumed orthogonal and stationary—in particular, Cartesian in this paper—and the transformed horizontal coordinates of computational domain $(\bar{x},\bar{y})$ are independent of the vertical coordinate z. The transformation in Eq. (1) is sufficiently flexible to accommodate a broad class of flows and underlying fluid equations, in a variety of domains on scales from laboratory and wind tunnel, through terrestrial environments and climate, to stellar [11]. Here, we employ incompressible Boussinesq approximation suitable for studies of atmospheric boundary layers [15] and dispense with many complexities of EULAG's theoretical formulation. Assuming neutral (nonbuoyant) and nonrotating boundary layer flows, the adopted Boussinesq equations can be compactly written (in physical space) as

$$\nabla \cdot (\rho_o \mathbf{v}) = 0,$$

$$d\mathbf{v}/dt = -\nabla \pi' + \mathcal{D}(\mathcal{E},\nabla \mathbf{v}),$$

$$d\mathcal{E}/dt = \mathcal{S}(\mathcal{E}). \tag{2}$$

Here $d/dt = \partial/\partial t + \mathbf{v}\cdot\nabla$; $\mathbf{v}$ denotes the velocity vector. The subscript $_o$ refers to the static reference state with constant density ρ_o and pressure $p_o = p_o(z)$, whereas $\pi' = (p-p_o)/\rho_o$. The $\mathcal{D}$ term in the momentum equation symbolizes viscous dissipation, via the divergence of a subgrid-scale momentum flux. The corresponding eddy coefficient is proportional to the square root of the "turbulent kinetic energy" $\mathcal{E}$. The evolution equation of $\mathcal{E}$ in Eq. (2) symbolizes the standard prognostic "TKE" subgrid-scale model, with all usual sinks and sources combined in the $\mathcal{S}(\mathcal{E})$ term on the right-hand side; see [15,18] for discussions. Alternatively, when eddy coefficients are arbitrarily prescribed, then prognostic TKE equation is dismissed.

For the purpose of this study, the governing Eq. (2) are cast in transformed coordinates—see Sec. II C for brief discussion and [12–14] for complete tensorial exposition—conforming to the evolving shape of the lower boundary

$$\bar{t} = t, \quad \bar{x} = x, \quad \bar{y} = y,$$

$$\bar{z}(x,y,z,t) = H_0 \frac{z - h(x,y,t)}{H_0 - h(x,y,t)}, \tag{3}$$

where h is the solid/fluid interface profile, and H_0 denotes the vertical extend of the fluid model domain. The transformation (3) is driven by the solution of the sediment motion model, discussed next.

B. Sediment motion model

The evolution of the solid/fluid interface is governed by the conservation law

$$\rho_s \, \partial h/\partial t + \nabla_H \cdot \mathbf{q} = 0, \tag{4}$$

where $\rho_s = \rho_m(1-\lambda)$ is the bulk density of the sediment with ρ_m and λ denoting, respectively, the density of the grain material and the porosity (volume fraction of voids), $\nabla_H = (\partial/\partial x, \partial/\partial y)$, and $\mathbf{q}$ is a vertically integrated sediment mass flux. In usual Aeolian transport where sand is the prevailing fraction of the grain mixture, the sediment flux $\mathbf{q}$ is ascribed to the saltation, a process that includes particle-size scale direct momentum transfer from the fluid to the grains and ejection due to grain collisions [16].

The template formula with the saltation flux value proportional to the cube of the friction velocity—a seminal contribution of Bagnold [19]—assumes the *saturation* condition defined by the equilibrated total momentum transfer from the air to the grains; see [16,20] for alternative constitutive models of saltation. Over the years, the Bagnold law has been adjusted to account for the critical dependence of the saltation transport on the friction velocity [21] and variable flow direction; see [6,7,21,22] for discussions. The adjusted formula can be written as

$$\mathbf{q}_S = C \frac{\rho}{g} \mathbf{u}_* \|\mathbf{u}_*\|^2 \max\left(0, 1 - \frac{u_t}{\|\mathbf{u}_*\|}\right). \tag{5}$$

Here, $\mathbf{q}_S$ is the saltation flux vector; C is an empirical coefficient [21]; ρ is the air density; $g = |\mathbf{g}|$ where $\mathbf{g}$ is the accel-

eration of gravity; $\mathbf{u}_* \equiv u_* \mathbf{v} \|\mathbf{v}\|^{-1}$ where the friction velocity $u_* = \sqrt{\rho^{-1} \tau_w}$, while τ_w denotes the wall shear stress. The threshold value u_t of the friction velocity, which already accounts for the angle γ between local wind and slope [7], is given as

$$u_t = \sqrt{\frac{\sin\theta}{\tan\alpha}\cos\gamma + \sqrt{\frac{\sin^2\theta}{\tan^2\alpha}(\cos^2\gamma - 1) + \cos^2\theta}\, u_{t0}}, \tag{6}$$

where θ is the local slope angle, α is the angle of friction, and u_{t0} is the threshold friction velocity for a flat bed [23].

The saltation flux alone is insufficient for representing realistic dune development. Similar to pile surface dynamics [17], sand dunes are subject to self-organized criticality [24,25], where upon reaching the critical slope ($s_C \equiv \tan\alpha = 0.625$ for sand) local grain avalanches discharge particle steepest descent to stabilize the slope; see Fig. 1 in [7] for an illustration. In EULAG, accounting for the avalanches prevents the unbounded steepening of local slopes and, thus, the singularity of the transformation in Eq. (3).

Following [17], we represent the avalanche transport in the form of diffusion fluxes

$$\mathbf{q}_A = -\rho_s \mathcal{K} \nabla_H h, \tag{7}$$

with the diffusion coefficient $\mathcal{K}(\mathbf{x},t)$ depending critically on the local slope

$$\mathcal{K} \equiv \beta \max[0, \mathrm{sgn}(\|\nabla_H h\| - s_C)], \tag{8}$$

where β is the diffusivity value specified in terms of temporal and spatial resolution of the numerical model [7].

The total flux entering the mass conservation law (4) is a sum of $\mathbf{q}_S$ and $\mathbf{q}_A$. To facilitate the solution procedures, we cast Eq. (4) as an advection-diffusion equation

$$\frac{\partial h}{\partial t} + \nabla_H \cdot \mathbf{U} h = \nabla_H \cdot \mathcal{K} \nabla_H h \tag{9}$$

with the advective velocity $\mathbf{U}$ defined as

$$\mathbf{U} \equiv \frac{\mathbf{q}_S}{\rho_s h}. \tag{10}$$

Formally, Eq. (9) is equivalent to Eq. (4) for any such constant that $h - \mathrm{const} = h'$, because the singularity of $\mathbf{U}$, as $h \searrow 0$, is removable. In order to give $\mathbf{U}$ a unique physical interpretation, we define h with respect to horizontal reference level at the upper limit of nonerodible substrate. Hence, $\mathbf{U}$ is an average velocity over a potentially mobilized sand layer.

The advection-diffusion form (9) of the sediment motion model (4) not only benefits solution procedures but also aids interpretation of the results in Sec. III. Apart from a small-scale episodic dissipative term on the right-hand side—de facto also combinable into the advective flux; cf. Sec. 5.2 in [26] and references therein—Eq. (9) is a flux-form PDE governing advection of the h profile in a compressiblelike flow $\mathbf{U}(\mathbf{x},t)$ with, generally, $\nabla_H \cdot \mathbf{U} \neq 0$. In the asymptotic limit of constant $\mathbf{U}$, which coincides with the limit of the migration speed defined in Eq. (2) of [27], Eq. (9) implies the translation of h without a change in shape. For fixed geometric length scales of the profile—respectively, h_o and a in the vertical and the horizontal—it follows from Eq. (10) that the resulting time scale of the profile translation $a/\|\mathbf{U}\|$ can be manipulated by altering magnitudes of the saltation flux $\mathbf{q}_s$ and/or the bulk sediment density ρ_s. Furthermore, each of the two may be varied by different means, thus offering a number of options for physical interpretation and their eventual relevance to laboratory realizations. However, from the perspective of numerical simulation this is an auxiliary issue. The key assumption behind our severe-wind scenario is that judiciously accelerating the evolution and migration of dunes does not obscure the physics of natural phenomena—an assumption that is only justified by expediency and ultimately by comparison with observations.

C. Numerical model

The governing Eq. (2) are solved numerically using a nonoscillatory forward-in-time (NFT) approach, widely documented in the literature; see [28] for a succinct review. Below we comment briefly on the essential aspects of the numerical solution procedure while referring the reader to earlier works for further details.

The evolution equations in Eq. (2), for each velocity component and $\mathcal{E}$, can be all written in the form of an Eulerian conservation law

$$\frac{\partial \rho^* \psi}{\partial \bar{t}} + \bar{\nabla} \cdot (\rho^* \bar{\mathbf{v}}^* \psi) = \rho^* R, \tag{11}$$

where ψ symbolizes the components of $\mathbf{v}$ or $\mathcal{E}$, and R stands for the corresponding right-hand sides. Furthermore, $\rho^* \equiv \rho_o \bar{G}$ with $\bar{G}$ denoting the Jacobian of the transformation (1); $\bar{\nabla} \cdot \equiv \partial / \partial \bar{\mathbf{x}} \cdot$, and $\bar{\mathbf{v}}^* \equiv d\bar{\mathbf{x}}/d\bar{t} \equiv \dot{\bar{\mathbf{x}}}$ is the *contravariant velocity* in the transformed space. An EULAG's template algorithm for integrating Eq. (11) to second-order accuracy (insofar as inviscid dynamics is concerned) over the temporal increment Δt can be concisely written as

$$\psi_{\mathbf{i}}^{n+1} = \frac{\rho^{*n}}{\rho^{*n+1}} \mathcal{A}_{\mathbf{i}}(\tilde{\psi}) + 0.5 \Delta t R_{\mathbf{i}}^{n+1}, \tag{12}$$

where $\psi_{\mathbf{i}}^{n+1}$ is the solution sought at the grid point $(\bar{t}^{n+1}, \bar{\mathbf{x}}_{\mathbf{i}})$, $\tilde{\psi} \equiv \psi^n + 0.5 \Delta t R^n$, and $\mathcal{A}$ denotes a two-time-level nonoscillatory finite-volume advective-transport operator; namely a fully second-order-accurate multidimensional positive definite advection transport algorithm (MPDATA); see [28] for a recent review. Subgrid-scale forcings included in R are first-order-accurate and explicit; cf. Sec. 3 in [29] for a discussion.

Equation (12) represents a system implicit with respect to pressure and all velocity components, because all principal forcing terms are assumed to be unknown at $n+1$. It is solved by employing the transformed mass-continuity constraint

$$\bar{\nabla} \cdot (\rho^* \bar{\mathbf{v}}^s) = 0, \quad \bar{\mathbf{v}}^s \equiv \bar{\mathbf{v}}^* - \partial \bar{\mathbf{x}} / \partial t. \tag{13}$$

Relation (12) written for components of $\mathbf{v}$ are transformed to

produce corresponding relations for components of the *solenoidal velocity* $\bar{\mathbf{v}}^s$ in Eq. (13). This leads to the elaborate boundary value problem for π', the complete exposition of which can be found in [12]; for symbolic operatorlike presentations see [29]. Boundary conditions imposed on $\bar{\mathbf{v}}^s \cdot \mathbf{n}$, subject to the integrability condition $\oint_\Sigma \rho^* \bar{\mathbf{v}}^s \cdot \mathbf{n} d\sigma = 0$, imply the appropriate boundary conditions on pressure [12,13]. The resulting elliptic problem is solved using a preconditioned nonsymmetric Krylov-subspace solver [30]. Given the updated pressure, and hence the updated solenoidal velocity, the updated physical and contravariant velocity components are constructed from the solenoidal velocity.

The metric and transformation coefficients embedded in Eq. (12) as well as the time derivative of the transformed coordinates in definition of Eq. (13) enter the solution procedure at t^{n+1} via R^{n+1} term on the right-hand side of Eq. (12) and via the elliptic solver. They are supplied by integrating the advection-diffusion PDE (9) over the double time step of the fluid model (effectively, from t^n to t^{n+2}) and then centering h and $\partial h/\partial t$ at t^{n+1}. An NFT integration of Eq. (9) to $O(\Delta t^2)$—see Sec. 3.2 in [7] for discretization details—suffices for second-order accuracy of the fluid model.

III. RESULTS

A. Design of experiments

A series of simulations is conducted for sand dunes evolving in uniform ambient wind $\mathbf{v}_e = (u_e, 0, 0)$. The initial shape of the lower boundary is assumed as a cosine sandpile

$$h(\mathbf{x}, t=0) = \begin{cases} h_o \cos^2\left(\dfrac{\pi r}{2a}\right) + h_b & \text{if } r/a \le 1 \\ h_b & \text{if } r/a > 1, \end{cases} \tag{14}$$

with height $h_o \in [0.5, 7.5]$ m and half-width a such that $h_o/a \approx 0.15$. The pile (14) is centered at $(x_o, y_o) = (L_x/3, L_y/2)$ of the Cartesian model domain $L_x \times L_y \times L_z$; $r \equiv \sqrt{(x-x_o)^2 + (y-y_o)^2}$; and h_b denotes the thickness of the sand layer underneath the pile (bed). Both $h_b = 0$ and $u_e = 11$ ms^{-1} are kept fixed in the present experiment. In the fluid model, for the upper boundary the impermeable free-slip lid is assumed, whereas lateral boundaries are open and periodic in the streamwise and spanwise direction, respectively. The initial condition assumes $\mathbf{v}(t=0) = \mathbf{v}_e - \nabla\phi$, with the potential perturbation ϕ determined from mass continuity and the boundary conditions imposed. In the sediment model, the boundary conditions are compatible with the governing form (9) and consistent with the fluid model. In particular, periodicity is assumed in the spanwise direction and, consistent with assuming $h_b = 0$ in Eq. (14), zero sediment flux at the inflow boundary. The initial condition of the sediment model is the lower boundary shape (14) of the fluid model.

The physical size of the model domain as well as selection of numerical parameters can be different for each simulation in the series. First, the grid resolution $N_x \times N_y \times N_z$ of a regular mesh (in the transformed computational space) is a compromise between the overall accuracy of integration and the affordability of lengthy massively-parallel calculations.

TABLE I. Evolutionary barchan dunes experiment.

h_o (m)	H (m)	Δt (s)	t_f/T_o
7.5[a]	9.7	0.05	232848
6.0[a]	7.6	0.03	174636
3.0[a]	3.7	0.02	232848
1.5[a]	1.6	0.01	209088
1.0[a]	1.0	0.005	121176
0.7[b]	0.6	0.002	105494
0.5[b]	0.4	0.002	105494

[a]Stable and metastable forms.
[b]Unstable forms.

Second, the physical size of the domain depends on dune speed (celerity) to assure the solution observability over a number of characteristic time scales. Third, the physical domain size and thus the corresponding grid increments are scaled with h_o to maintain a uniform numerical accuracy throughout the series of simulations. Among seven simulations discussed below, five are for dunes reaching an equilibrium and two for unstable forms. In the first case, the model domain $L_x \times L_y \times L_z = 46h_o \times 32h_o \times 5.3h_o$ is resolved with a $171 \times 119 \times 41$ grid. In the second case, the domain $96h_o \times 32h_o \times 5.3h_o$ is covered with a $333 \times 119 \times 41$ grid. In both cases, the grid increments are $\Delta x = \Delta y \approx 0.27h_o$, and $\Delta z \approx 0.132h_o$, respectively, in the horizontal and the vertical. The temporal increment Δt, which assures uniform numerical accuracy by maintaining a constant Courant number at ≈ 0.5, is listed in Table I together with the initial pile height h_o, the final observed height H of the landform, and the dimensionless final time of calculation t_f/T_o where $T_o = a/u_e$; Fig. 1 defines the geometric characteristics of dunes, used consistently throughout the paper.

The remaining simulation parameters are as follows. The surface drag coefficient in the Smagorinsky-type subgrid-scale model [15] is $C_D = 0.01$. In the avalanche scheme (8) the diffusivity $\beta = 0.0625[\min(\Delta x, \Delta y)]^2/\Delta t$, see Sec. 4.1 of [7] for discussion. In the saltation flux formula (5) the friction velocity $\mathbf{u}_*$ is evaluated from the logarithmic law

$$\mathbf{u}_* = \kappa \frac{(\mathbf{v} - \mathbf{v}\cdot\mathbf{n})\big|_{z_\Delta}}{\ln(z_\Delta/z_0)}, \tag{15}$$

where z_Δ is the distance between the surface and the adjacent model level, cf. [6], and z_0 is an equivalent roughness length

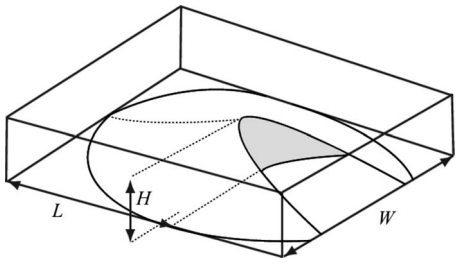

FIG. 1. Sketch of a dune: H, height (measured from base to brink); W maximal width; L length (excluding horns).

(accounting for the flow-to-grains momentum transfer) taken as $z_0=0.001$ m, and $\kappa=0.41$ is the von Karman constant. The sediment transport parameters are as follows. The empirical coefficient $C=4.2\sqrt{d/D}$, where d is the average actual grain size, and $D=0.25\times10^{-3}$ m refers to the standard grain size; cf. Eq. (8) and Table I in [31] or pp. 113–114 in [32]. The value of $C=5.5$ is typically assumed in the literature; e.g., [6]. It corresponds to the average grain size of approximately 0.4×10^{-3} m, consistent with the authors' own measurements in the Great Sand Dunes National Park.

To realize the severe-wind scenario, a key premise of this study, we multiply $\mathbf{q}_S$ by the factor of 1440; thereby simulating a day of real dune lifetime in the model minute. Furthermore, the density of the quartz $\rho_m=2650$ kg/m^3, and the porosity $\lambda=0.5$. In Eq. (6) the horizontal threshold friction velocity is $u_{t0}=0.22$ m s^{-1} after [23]. This value is consistent with the authors' measurements in the Sand Dunes National Park, which document the lack of appreciable particle motion for shear velocities below the adopted threshold, but a 0.05–0.10 m height of bounce of sand particles observed for wind velocity of about 16 miles per hour measured at 0.15 m above the bed. The latter is consistent with the theoretical estimate $z_{\max}\approx(w)^2/g$ [33], assuming vertical velocity w of the same order as the shear velocity.

B. Evolution of an isolated barchan dune

The development of an isolated barchan dune on a noneroodible bed—a canonical problem in the study of evolutionary sand dune dynamics [4,6,19,33]—still eludes complete understanding and consistent results [9]. To introduce the synthesis of the series of simulations described in the preceding section, Fig. 2 features the transformation of a sandpile with an initial height $h_o=7.5$ m into a barchan dune, over 36 min of simulated time with 12 min interval. The figure corresponds to Fig. 2 in [7] that displays the analogous result for $\lambda=0$, and thus twice larger bulk sediment density ρ_s in Eq. (4), over 72 min of simulated time with 24 min interval. Although the two results differ in fine details (e.g., compare the tips of horns at the latest times), the close agreement of the shape and position of the evolving dune in two simulations verifies the severe-wind scenario.

Figures 3 and 4 complement the dune surface evolution in Fig. 2 with the display of the instantaneous boundary layer flow (isolines of vertical velocity and flow vectors), in the central vertical plane and at the lower surface, respectively, superimposed with the evolving dune profile. Together, Figs. 2–4 document that on the windward side the simulated dune is defined over a compact support, free of sand residual trailing just upwind of the base. Such an unphysical sand deposition at the base of the windward slope is troublesome in numerical modeling of barchan dunes [4,6,16]. It is often attributed to the saturation assumption underlying the Bagnold model (5); see Sec. VII in [16] for a comprehensive discussion. The authors in [4] (Sec. III B) argue that with a saturated saltation flux the incompressible mass continuity equation inevitably leads to the positive $\partial h/\partial t$ at the windward side. In contrast, the "minimal model" in [16] relaxes the saturation assumption, and is free of the aforementioned

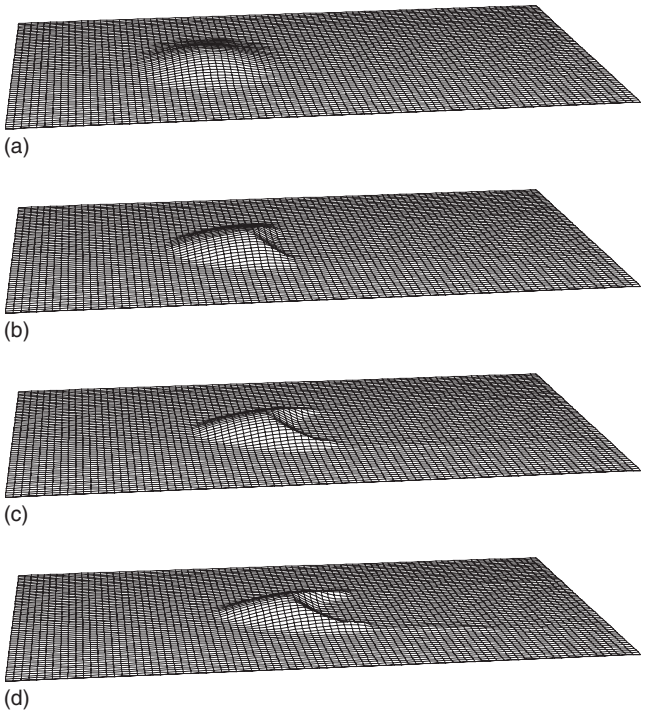

FIG. 2. Evolution of a barchan dune (surface shape) in a prevailing wind from left to right.

artifact. Because our saltation model is, in essence, the same as those used in [4,6], our prediction free of the artifact warrants a comment. First, consider that the full coupling of the fluid dynamics and the evolutionary landform incorporates the term $\propto\partial h/\partial t$ in the mass continuity (13). This augments the arguments of [4] and makes the problem in Eq. (9) implicit in $\partial h/\partial t$, with saturated saltation flux $\mathbf{q}_S$ depending (via $\mathbf{u}_*$) not only on h but also on its time derivative. Second, consider that casting the saltation flux (5) in an advective form, while integrating the resulting PDE (9) using a finite-volume upwinding [26,28], requires provision of transportive velocities at faces of computational cells—e.g., $U_{i+1/2}=(q_S|_{i+1}+q_S|_i)/(h_{i+1}+h_i+\epsilon)$ for a 2D problem on a Cartesian grid. The transportive velocity combined into the advective flux of upwinding—e.g., $Uh|_{i+1/2}=\max(0,U_{i+1/2})h_i+\min(0,U_{i+1/2})h_{i+1}$ for a 2D Cartesian grid—regularizes the analytic flux (5) with a factor $\sim 2h(x)/[h(x)+h(x+\Delta x)+\epsilon]=1+O(\Delta x)$. Due to the positivity of the numerics (ensuring $h\geq0$ via customized flux limiting, see Sec. 3.2 in [7]) the latter assures $\mathbf{q}_S\to0$ as $h\searrow0$. This does not controvert the arguments on the inadequacy of the saturated influx at the foot of the dune (Sec. VII of [16]) because the effecting numerical flux can become locally unsaturated in response to physical constrains built in the NFT numerics.

C. Scale dependence

The evolution in Figs. 2–4 is representative of the series of results obtained for various sizes of the initial sand pile. Figure 5 summarizes the series with a display of dune celerity U, length L, and width W in function of its height H; cf. Fig. 1 for corresponding definitions. The celerity is expressed

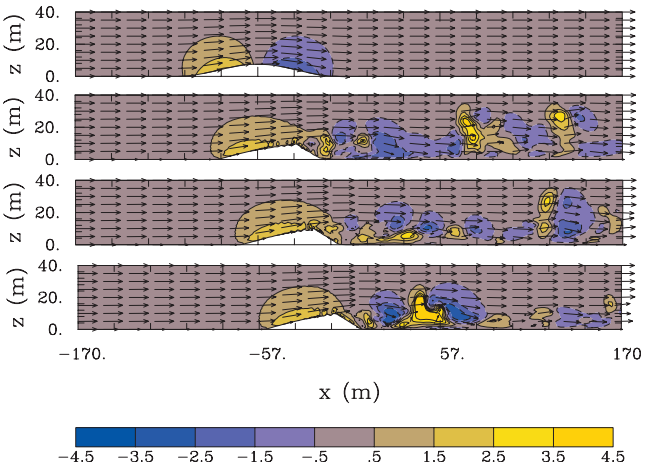

FIG. 3. (Color) Vertical velocity in the central xz plane.

in meters per day, by accounting for the correspondence of the model minutes to days of natural dunes time. For stable forms—entries[a] in Table I—the values of all variables represented in Fig. 5 were taken after the shape and celerity stabilization. However, for the unstable forms—entries[b] in Table I—all the values were evaluated as time averages.

The predicted values of H and U fit the curve $U=c/(H-b)$, also included in Fig. 5. For U and H taken in units of m/day and m, respectively, $c=18$ m^2/day, and $b=0.3$ m. The resulting curve is consistent with the Bagnold classical relation $U\propto H^{-1}$ [19]. The selected results fall in the range obtained in other computational studies. For instance, the celerity of the largest dune, the evolution of which is displayed in Figs. 2–4, is roughly half of that reported in [6] and close to value quoted in [4]. The existing field and experimental data are sparse and recorded for a disperse range of initial and ambient conditions. Although our results may depart from the measured values, they appear congruent with the data; see Fig. 8 in [33] and references therein. Moreover, the approximate linear dependence of W and L on H, $L\approx W\approx 7H+3.8$, shown as the solid line in Fig. 5, is consistent with the data in Figs. 3 and 4 in [33] (the accuracy of interpreting numerical data is addressed in the Appendix). It enables the alternative scalings advocated in the literature [9,27]; e.g., $U(L)=c/(L+b)-p$ with $c=337$ m^2/day, $b=1.1$ m and $p=4$ m/day. While the data in [33] show that small and large dunes may not be homothetic, our calculations seem to indicate dune *self-similarity*, at least for $h_o\leq 4$ m. For illustration, the instantaneous solutions for $h_o=3$ and 1 m are juxtaposed in Fig. 6; the respective solution instants, $T/t_o=76032$ and 14256, were selected soon after the dune shape has stabilized (cf. Fig. 7). The corresponding shape-defining values are as follows: $H=3.7$ and 1.05 m; $W=30$ and 10.3 m; $L=27$ and 9 m; and $W/L=1.12$ and 1.14. The self-similar initial conditions assumed in Eq. (14) provide likely the simplest explanation for the disparity between our results and observations summarized in [9,33]. We shall return to this point later in this section.

Figure 7 shows the history $H/h_o(t/T_o)$ for various h_o. For sandpiles with $h_o\geq 3$ m the stabilization is evident. For $h_o=1$ and 1.5 m a slow decay is observed after the initial stabilization, which increases dramatically for $h_o=0.5$ m; the

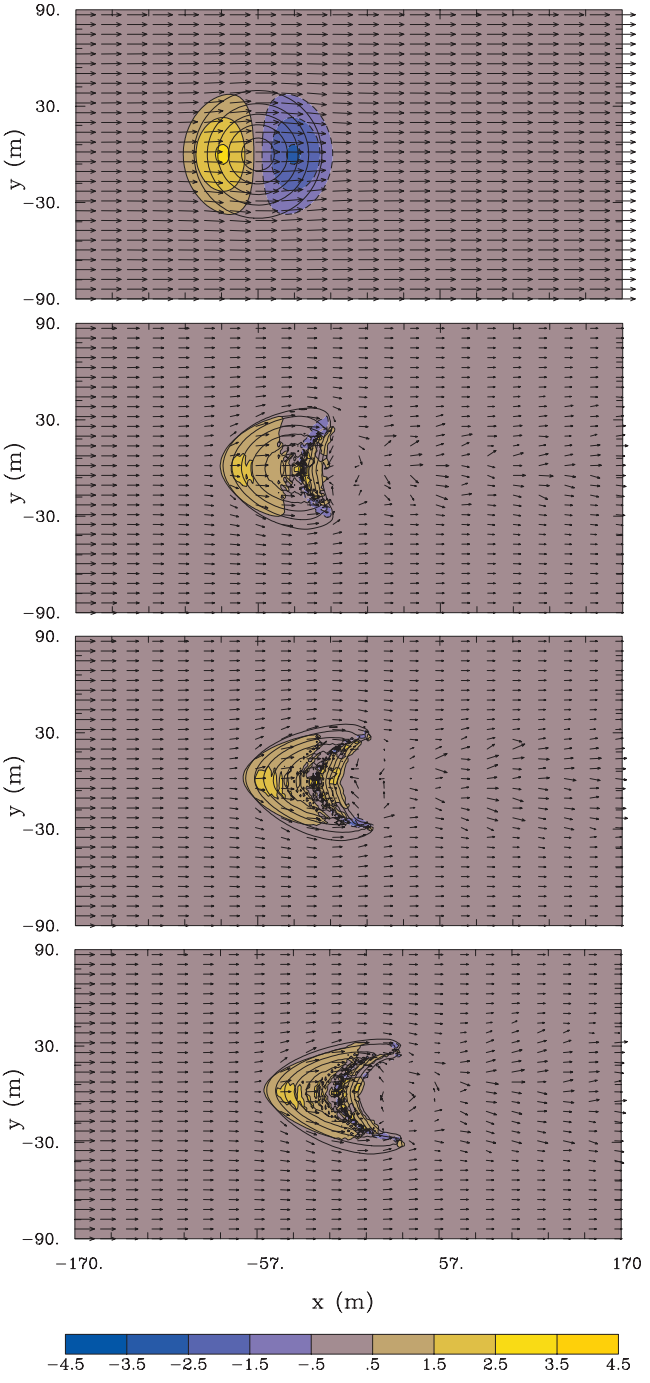

FIG. 4. (Color) Surface vertical velocity with superimposed isolines of the actual dune elevation; cf. Fig. 3.

evolution rates are purposely exaggerated by the scaling adopted. For sandpiles smaller than 1 m, the decay is concomitant with a progressive shape elongation (not shown), ultimately leading to sandpile "blow out," in agreement with experimental data; see Fig. 7 in [33]. This validates the adopted severe-wind scenario and the sediment-motion model (9). The minimum dune size depends critically on the *saturation length* l_{sat}—defined as a Lagrangian distance required for grain-bed-wind microdynamics to reach the saturation—such that $L>l_{\mathrm{sat}}$ forms a necessary condition of dune stability (Bagnold [19], pp.183). The saturation length

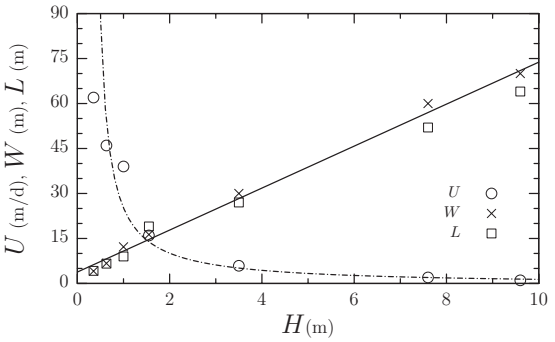

FIG. 5. Dune celerity U, width W, and length L in function of height H.

is proportional to the ratio of sand and air densities and to grain diameter [19]. Taking the average grain size as 0.4 mm, $l_{sat} \approx 10.6$ m. According to Fig. 5 and Table I, the latter value exceeds L for $h_o \lesssim 1$ m, in agreement with the observations [19,33].

The shape stabilization reached in our experiments coincides with the formation of self-similar barchan dunes (for initial pile heights higher than approximately 1 m) after very different transients. The observed self-similarity of numerical

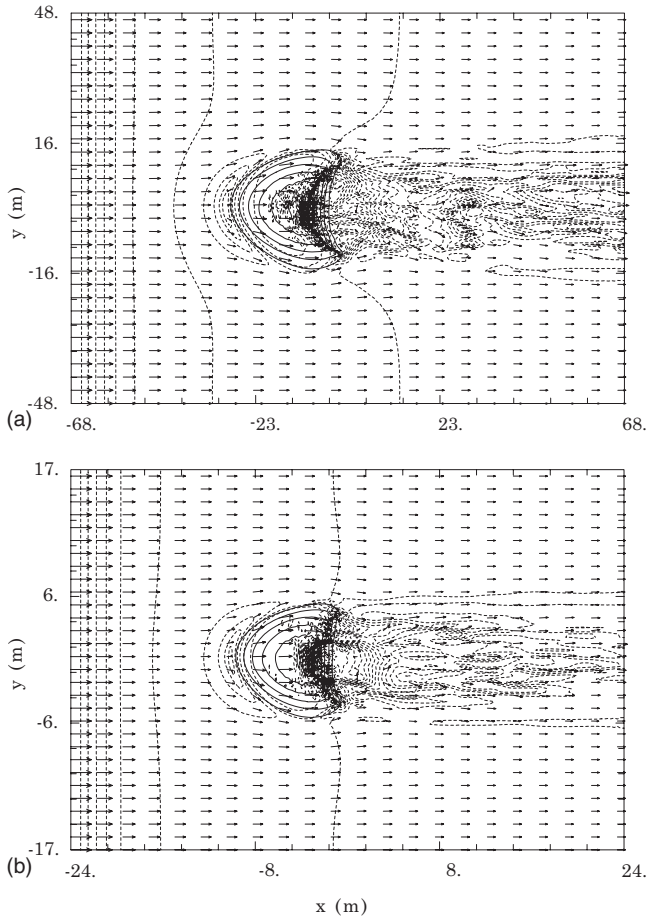

FIG. 6. Instantaneous flow along the dune surface for h_o3.5 m (top) and 1.0 m (bottom); isolines of streamwise perturbation velocity component $(u-u_e)$ with superimposed horizontal flow vectors

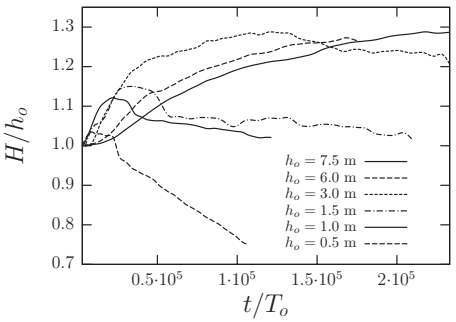

FIG. 7. Dune height in function of time.

solutions appears consistent with predictions from the minimal model of Kroy *et al.* [27] that sufficiently large dunes evolving from a similar initial profile are asymptotically scale invariant (see their Fig. 13). On the other hand, dunes of the same mass reach the same asymptotic shape regardless of the initial profile (their Fig. 17). Together, the two results imply that to the first approximation the shape of natural barchan dunes is predetermined, in accord with experience of casual observers. For completeness, we repeated the reference simulation of Sec. III B in two spatial dimensions and conducted two additional 2D runs with the parameters of the initial sandpile (14) altered, such that $(h_o,a)=(5,75)$ m and $(10,\ 37.5)$ m preserve the "mass" of the $(h_o,a)=(7.5,50)$ m reference profile. The results in Fig. 8 are consistent with those in Fig. 17 of [27]. The initial piles with $h_o=10$ and 7.5 m reach the characteristic asymptotic forms with maximum heights 9.6 and 9.2 m, respectively; whereas in the same time, the 5 m pile reaches only 6.1 m height, still

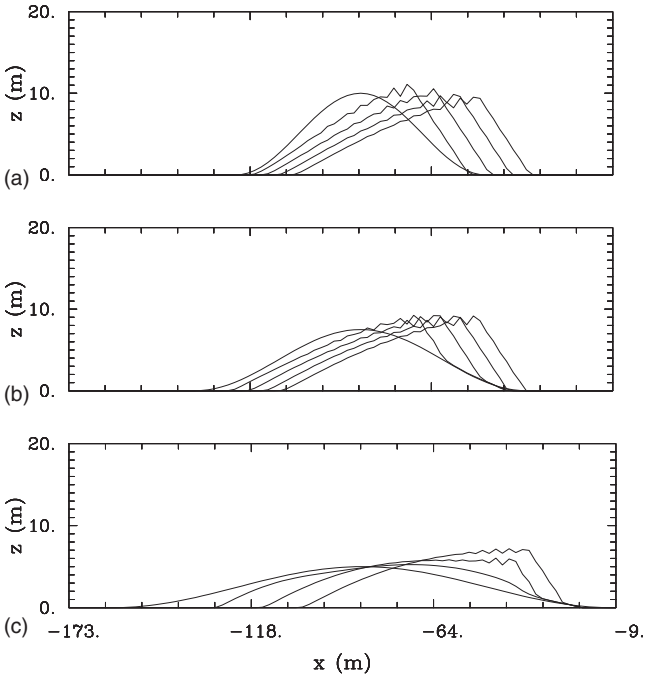

FIG. 8. Evolution of the surface profiles for 2D dunes of equal mass. The simulated time interval between consecutive profiles is $\delta t=4$ min in the two upper panels, but twice larger in the bottom panel.

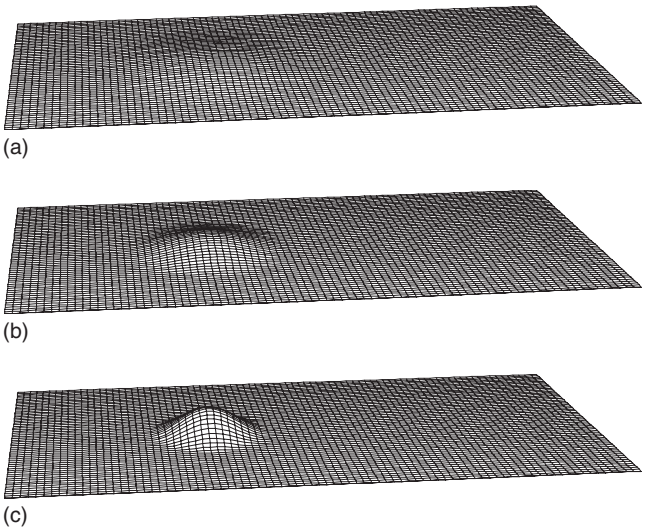

FIG. 9. Initial sandpiles of equal mass but different initial heights and half-widths.

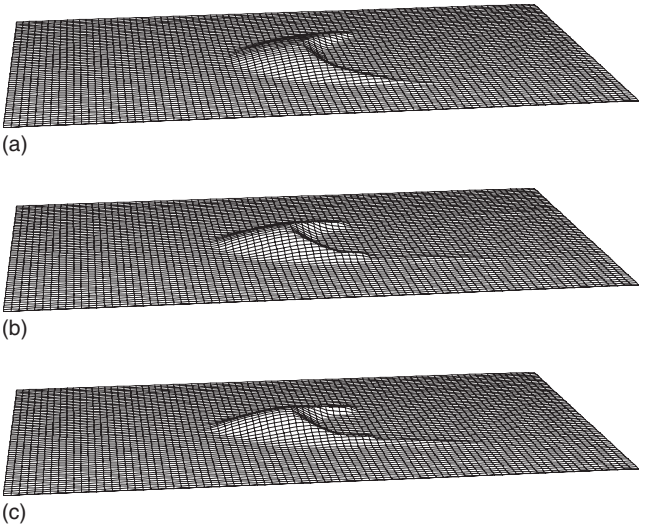

FIG. 10. Equilibrated barchan dunes of equal mass but different initial heights and half-widths; $t=36$ min.

transitioning to the asymptotic stage (cf. upper panel in Fig. 17 of [27]).

The remarkable shape invariance of barchan dunes owes much to the topology of thermally homogeneous boundary-layer flow over gently sloped obstacles. Such flows are predominantly 2D with relatively small variability in the horizontal—an anisotropy aspect already captured by the potential-flow solutions. With increasing steepness of the obstacle, or increasing stability of ambient stratification, more flow tends around the obstacle (which is also true in the potential-flow limit) evincing a richness of intricate realizations [34–36]. To illustrate the effect of three dimensionality, we varied the 3D reference run such as to preserve the mass of pile (14). Figure 9 shows the initial sandpiles with heights and half-widths $(h_o,a)=(3.75,50\sqrt{2})$, (7.5, 50) and $(15.,50/\sqrt{2})$ m; whereas the evolved surface profiles after 36 min of simulation are shown in Fig. 10. A close examination of the results reveals that the flat initial pile evolves into a broader dune with $(H,W,L)=(7.5,90.0,52.5)$ m, whereas the steep pile transforms into a more elongated dune with $(H,W,L)=(10.5,66.8,62.3)$; the shape resulting from the reference pile $(H,W,L)=(9.7,71.3,57.0)$ stays in between but closer to the steeper form. Furthermore the flatter dune tends to migrate slightly faster than the elongated one, which appears consistent with enhanced 3D effects causing less flow to go over, and more around, the steeper obstacle. For completeness, the evolution of the three dunes is quantified in the Appendix.

IV. EXTENSIONS

Much of understanding of Aeolian dunes comes from computational models. However, the majority of such models tend to focus on the sediment transport while assuming some phenomenological description of the atmospheric flow. The assumption common to all phenomenological models is an ensemble average flow representation, or, alternatively, solution of the so-called Reynolds-averaged Navier-Stokes' (RANS) equations. The development proposed in this paper is distinct, as it relies on (but is not limited to, cf. [11].) the large-eddy simulation approach that admits flow intermittency and instantaneous adaptation to ever-changing ambient conditions, the lower boundary shape in particular [37]. The numerical model adapted for the present study is a derivative of an extensive research on numerical simulation of weather and climate processes. Naturally, it contrasts with established models for computing Aeolian dunes by emphasizing the atmospheric boundary layer component. Notwithstanding, the results presented attest to its veracity, even though it currently employs a relatively basic formulation of the sediment transport. On the other hand, its versatility proven with a variety of complex atmospheric, oceanic, and laboratory flows opens avenues for research of mesoscale desert environment.

To substantiate the latter statement and to illustrate the potential of the approach, we conclude the paper with an application likely never addressed in the literature, yet realizable in nature in various contexts. Here we consider the evolution of an isolated sandhole, a canonical model for practical problems of well preservation and trafficability maintenance. The negative of the initial sandpile in Eq. (14) with $h_o=-7.5$ m is embedded in a $h_b=7.5$ m bed; hence, the sediment model assumes $\partial\mathbf{U}/\partial\mathbf{n}=0$ in Eq. (10) and $h=h_b$ in Eq. (14) at the inflow boundary. The ambient wind is the same as in barchan simulations. In analogy to Fig. 2, Fig. 11 features the evolution of a sandhole over 36 min of simulated time with 12 min interval. The corresponding Fig. 12 shows the instantaneous boundary layer flow in the central vertical plane. At a glance the evolution of a sandhole appears to bear little similarity to the evolution of a sandpile (Figs. 2–4); see also the evolution of an equivalent barchan dune on the erodible bed, Figs. 4 and 5 in [7].

The qualitative aspects of the sandhole transformation may be traced back to a viscous flow past a stationary hole, in the same spirit as the transformation of a barchan dune can be deduced from the properties of viscous flow past a hill; cf. [27,33]. At $t=0$ the flow is potential and essentially mirrors

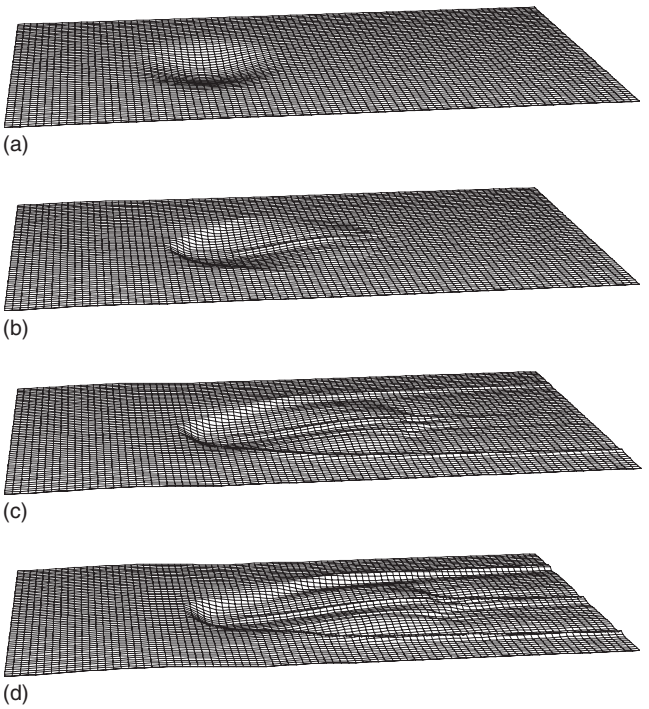

FIG. 11. Evolution of a sandhole; surface shape at the times of Fig. 2.

the flow past a pile; compare the uppermost plates of Figs. 12 and 3. Moreover, while the initial flow past a pile is slightly deflected outward, the flow past a hole bends gently inward sinking in to the hole. At $t=12$ min the flow is already fully developed with a characteristic recirculation region on the leeward face of the hole (second plate from the top of Fig. 12). To assess the role of fluid dynamics in the evolution of the sandhole, we conducted an analogous simulation past a stationary hole, $h(x,y,t)=h(x,y,0)$ in Eq. (3), and diagnosed the eventual surface perturbation that would occur if the surface of the stationary hole were allowed to evolve according to Eq. (4).

Figure 13 shows the hypothetical surface perturbation, together with vectors of the corresponding saltation flux, at t

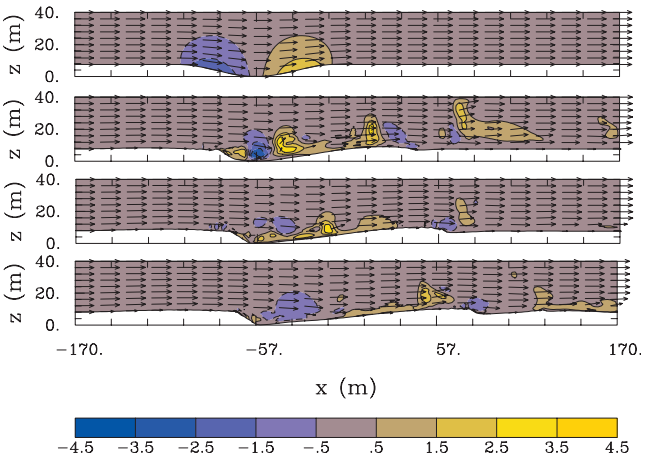

FIG. 12. (Color) Evolution of a sandhole; vertical velocity w in central xz plane at times of Fig. 11.

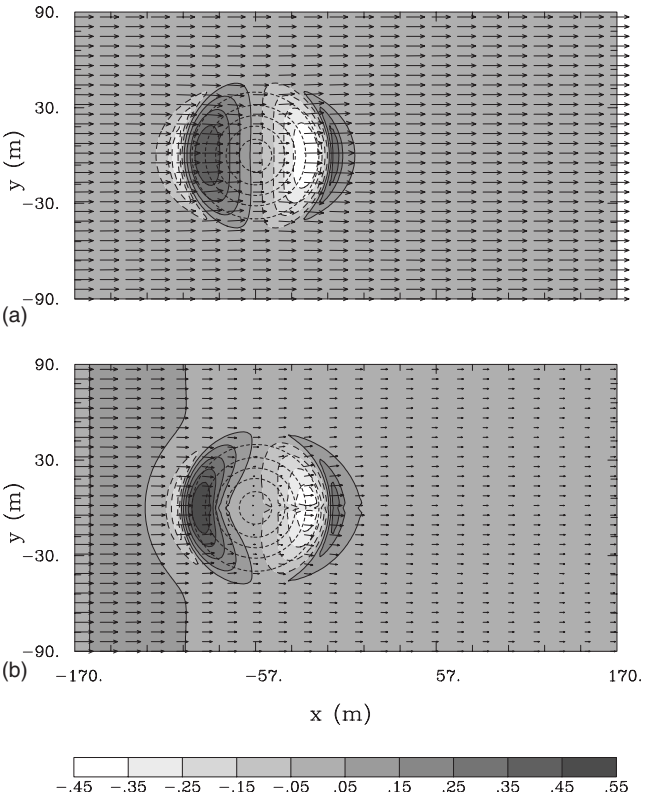

FIG. 13. Hypothetical surface perturbation $\delta t(\partial h/\partial t)$ with superimposed vectors of the corresponding saltation flux $\rho_s^{-1}\mathbf{q}_S$ at $t=0$ (upper plate) and $t=6$ min (lower plate); the arrow length of the undisturbed flux corresponds to 0.2 $m^2\ s^{-1}$, and $\delta t=1$ min.

$=0$ and $t=6$ min; by the latter time the flow past the stationary hole is essentially steady. The upper plate in the figure shows that the large-scale aspects of the sandhole evolution—such as the propagation of the leeward and windward faces, and the emergence of a secondary pile downwind—are already predetermined by the potential flow solution. The superimposed viscous effects show the tendency for enhancing the streamwise asymmetry of the prob-

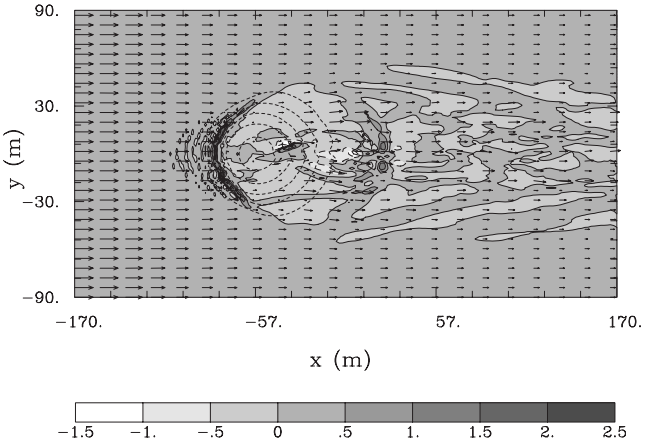

FIG. 14. Actual instantaneous surface perturbation $\delta t(\partial h/\partial t)$ and vectors of the corresponding saltation flux $\rho_s^{-1}\mathbf{q}_S$ at $t=6$ min of the sandhole evolution; δt and the arrow length of the undisturbed flux are the same as in Fig. 13.

TABLE II. Evolution of barchan dunes with an equal mass.

t [a]	0	6	12	18	24	30	36	42
H [b]	3.8	3.8	4.5	5.3	5.6	6.8	7.5	7.5
W [b]	100.1	102.8	98.3	93.9	91.6	90.0	90.0	90.0
L [b]	100.1	86.3	76.9	71.3	65.3	56.3	52.5	52.5
δX [b]	0.0	9.0	9.0	22.5	49.5	52.5	55.5	61.5
H [c]	7.5	9.0	9.8	10.1	10.5	10.1	10.1	9.7
W [c]	79.5	78.0	75.0	72.8	71.3	71.3	71.3	71.3
L [c]	79.5	69.0	61.5	57.8	57.0	57.0	57.0	57.0
δX [c]	0.0	18.0	24.0	27.8	33.8	40.5	47.3	54.8
H [d]	15.0	14.3	12.8	12.0	11.6	11.3	10.5	10.5
W [d]	60.8	62.3	63.8	65.3	65.3	66.4	66.8	66.8
L [d]	60.8	60.0	60.0	60.8	61.1	61.5	62.3	62.3
δX [d]	0.0	11.3	18.0	25.5	33.0	39.8	48.0	55.5

[a] t in minutes of simulated time; H, W, and L in meters.
[b] Flat dune $(h_o,a)=(3.75,50\sqrt{2})$ m.
[c] Reference dune $(h_o,a)=(7.5,50)$ m.
[d] Steep dune $(h_o,a)=(10,50/\sqrt{2})$ m.

lem, with the characteristic steepening in the vertical and arching in the horizontal the leeward face of the sandhole, analogously to the slip face of a barchan dune.

Although the elemental simulation past a stationary hole provides insights to key tendencies of the landform evolution, it is hardly instructive in so far as timing, magnitude and fine-scale features of the evolving surface are concerned. This is illustrated in Fig. 14 that shows the actual instantaneous sediment transport at $t=6$ min of the sandhole evolution.

Apart from illustrating the cognitive power and versatility of atmospheric/oceanic LES fully coupled with evolutionary landform underneath, the highlighted pilot study revealed interesting similarities as well as disparities of sandhole and dune evolutions. For example, the speed of sandhole migration increases as it size decreases, yet small sandholes evolve into elongated shapes reminding sandpiles blown out without a sand supply; Fig. 7 in [33]. Furthermore, in the spirit of colliding dunes [38–40], sandholes interact in a complex manner depending upon their relative sizes. However, the migration speed of the leeward face substantially slower than the propagation of the secondary pile (Figs. 11 and 12) adds intricacy unseen for colliding dunes. Interaction of sandholes is particularly intriguing as it may provide a viable hypothesis on the formation of continuous fields of dunes (not to be confused with fields of isolated barchans; Fig. 1 in [41]) characteristic of mesoscale desert topography; Fig. 4 in [17]. Inasmuch as initializing continuous dune fields with isolated sandpiles may be difficult to reason, an initial condition consisting of isolated sandholes seems more plausible; e.g., as an effect of a meteorite shower, or due to sunken roads and engineering works in sandy desert regions. These and the related topics exceed the scope of the present paper, but they will be pursued and reported in future publications.

ACKNOWLEDGMENTS

We are grateful to our colleagues Charles A. Knight for helping with analysis of our sand samples, and Melvyn A. Shapiro for inspiring the sandhole problem. Comments from two anonymous referees helped to improve the paper. Computer time was provided by NSF MRI Grant No. CNS-0421498, NSF MRI Grant No. CNS-0420873, NSF MRI Grant No. CNS-0420985, NSF sponsorship of the National Center for Atmospheric Research, the University of Colorado, and a grant from the IBM Shared University Research (SUR) program. The National Center for Atmospheric Research is sponsored by the National Science Foundation. This work was partially supported by the DOE Award No. DE-FG02-08ER64535 and the MICIIN Grant No. BIA-2008-00522.

APPENDIX: EVOLUTION OF BARCHAN DUNES WITH AN EQUAL MASS

To convey the dynamics of 3D dunes highlighted in Figs. 9 and 10, here their geometric parameters H, W, and L (cf. Fig. 1) and the displacement δX of the apex are tabulated with simulated time interval $\delta t=6$ min. The heights $H(t)$ and displacements $\delta X(t)$ were read from largely magnified computer displays of panels such as those in Fig. 3. Similarly, the widths $W(t)$ and lengths $L(t)$ were read judiciously at $z=0.75$ (i.e., at $0.1h_o$ of the reference dune) from the displays of panels like those in Fig. 4. Note that although the half-width of the initial sandpiles decreases in proportion to $1/\sqrt{2}$ the scaling of their radii at $z=0.75$ is more intricate, because Eq. (14) implies the inverse relation

$$r = \frac{2a}{\pi}\cos^{-1}\left(\sqrt{\frac{z}{h_o}}\right). \quad \text{(A1)}$$

The alternative measures of L and W at $z \approx 0$ read from vertical cross sections in xz and yz planes can be $\lesssim 4$ m (or $\lesssim 7\%$) larger, for the big dunes considered here. On the other hand, the estimated error of measuring the numerical model output for H and δX translates to $\lesssim 0.4$ m (or $\lesssim 5\%$). Notably, the values of L in Fig. 5 were measured in central xz planes. To enable a range of further analyses, Table II lists dimensional values of H, W, L, and δX. The evolutionary trends depicted in the table are self-evident. Similarly like in the 2D case, summarized in Fig. 8, there is a tendency for the convergence toward a common asymptotic shape: the flat dune steepens and shrinks laterally, whereas the steep dune shrinks in the vertical and broadens laterally. Furthermore the final shapes and positions of the steep and the reference dunes are closer to each other than the final shapes and positions of the flat and the reference dunes. Notwithstanding, the actual shape of simulated 3D dunes shows the signature of initial conditions over the entire duration of numerical experiments.

[1] J. G. Venditti and S. J. Bennett, J. Geophys. Res. **105**, 22035 (2000).
[2] B. T. Werner, Geology **23**, 1107 (1995).
[3] H. Nishimori, M. Yamasaki, and K. H. Andersen, Int. J. Mod. Phys. B **12**, 257 (1998).
[4] W. S. Weng, J. C. R. Hunt, D. J. Carruthers, A. Warren, G. F. S. Wiggs, I. Livingstone, and I. Castro, Acta Mech. **2**, 1 (1991).
[5] V. Schwammle and H. Herrmann, Earth Surf. Process. Landf. **29**, 769 (2004).
[6] F. K. Wippermann and G. Gross, Boundary-Layer Meteorol. **36**, 319 (1986).
[7] P. Ortiz and P. K. Smolarkiewicz, Int. J. Numer. Methods Fluids **50**, 1229 (2006).
[8] P. Hersen, S. Douady, and B. Andreotti, Phys. Rev. Lett. **89**, 264301 (2002).
[9] C. Groh, A. Wierschem, N. Aksel, I. Rehberg, and C. A. Kruelle, Phys. Rev. E **78**, 021304 (2008).
[10] E. Buckingham, Phys. Rev. **4**, 345 (1914).
[11] J. M. Prusa, P. K. Smolarkiewicz, and A. A. Wyszogrodzki, Comput. Fluids **37**, 1193 (2008).
[12] J. M. Prusa and P. K. Smolarkiewicz, J. Comput. Phys. **190**, 601 (2003).
[13] N. P. Wedi and P. K. Smolarkiewicz, J. Comput. Phys. **193**, 1 (2004).
[14] P. K. Smolarkiewicz and J. M. Prusa, Int. J. Numer. Methods Fluids **47**, 789 (2005).
[15] L. G. Margolin, P. K. Smolarkiewicz, and Z. Sorbjan, Physica D **133**, 390 (1999).
[16] G. Sauermann, K. Kroy, and H. J. Herrmann, Phys. Rev. E **64**, 031305 (2001).
[17] L. Prigozhin and B. Zaltzmann, Phys. Rev. E **63**, 041505 (2001).
[18] U. Schumann, Theor. Comput. Fluid Dyn. **2**, 279 (1991).
[19] R. A. Bagnold, *The Physics of Blown Sand and Desert Dunes* (Methuen Ltd., London, 1954).
[20] J. P. Bouchaud, M. E. Cates, J. Ravi Prakash, and S. F. Edwards, Phys. Rev. Lett. **74**, 1982 (1995).
[21] K. Lettau and H. H. Lettau, in *Exploring the Worlds Driest Climate, Lettau and Lettau*, edited by H. H. Lettau and K. Lettau (University of Wisconsin, Madison, 1978).
[22] J. D. Iversen and K. R. Rasmussen, Sedimentology **41**, 721 (1994).
[23] D. A. Gillette, J. Adams, D. Muhs, and R. Kihl, J. Geophys. Res. **87**, 9003 (1982).
[24] P. Bak, C. Tang, and K. Wiesenfeld, Phys. Rev. A **38**, 364 (1988).
[25] H. M. Jaeger, C. H. Liu, and S. R. Nagel, Phys. Rev. Lett. **62**, 40 (1989).
[26] P. K. Smolarkiewicz and J. Szmelter, J. Comput. Phys. **206**, 624 (2005).
[27] K. Kroy, G. Sauermann, and H. J. Herrmann, Phys. Rev. E **66**, 031302 (2002).
[28] P. K. Smolarkiewicz, Int. J. Numer. Methods Fluids **50**, 1123 (2006).
[29] P. K. Smolarkiewicz, R. Sharman, J. Weil, S. G. Perry, D. Heist, and G. Bowker, J. Comput. Phys. **227**, 633 (2007).
[30] P. K. Smolarkiewicz, C. Temperton, S. J. Thomas, and A. A. Wyszogrodzki, *Proceedings of the ECMWF Seminar Series on Recent Developments in Numerical Methods for Atmospheric and Ocean Modeling, 2004, Reading, UK* (ECMWF, Reading, UK, 2004), pp. 203–220.
[31] A. D. Howard, J. B. Morton, M. Gad-El-Hak, and D. B. Pierce, Sedimentology **25**, 307 (1978).
[32] K. Pye and H. Tsoar, *Aeolian Sand and Sand Dunes* (Unwyn Hyman, London, 1990).
[33] B. Andreotti, P. Claudin, and S. Douady, Eur. Phys. J. B **28**, 321 (2002).
[34] J. C. R. Hunt, C. J. Abell, J. A. Peterka, and H. Woo, J. Fluid Mech. **86**, 179 (1978).
[35] J. C. R. Hunt and W. H. Snyder, J. Fluid Mech. **96**, 671 (1980).
[36] P. J. Mason and B. R. Morton, J. Fluid Mech. **175**, 247 (1987).
[37] For an illustrative distinction between LES and RANS, compare supplementary animation and Fig. 6 in the on-line version of [29].
[38] V. Schwammle and H. Herrmann, Nature (London) **426**, 619 (2003).
[39] N. Endo, K. Taniguchi, and A. Katsuki, Geophys. Res. Lett. **31**, L12503 (2004).
[40] P. Hersen and S. Douady, Geophys. Res. Lett. **32**, L21403 (2005).
[41] P. Hersen, K. H. Andersen, H. Elbelrhiti, B. Andreotti, P. Claudin, and S. Douady, Phys. Rev. E **69**, 011304 (2004).